



Flexible heat-spreading and air-cooling films using nickel-electroplated nanotextured fibers



Taegun Kim^{a,1}, Seongpil An^{b,1}, Chanwoo Park^a, Jeehoon Choi^c, Alexander L. Yarin^{d,*}, Sam S. Yoon^{a,*}

^a School of Mechanical Engineering, Korea University, Seoul 02841, Republic of Korea

^b SKKU Advanced Institute of Nanotechnology (SAINT) and Department of Nano Engineering, Sungkyunkwan University (SKKU), Suwon 16419, Republic of Korea

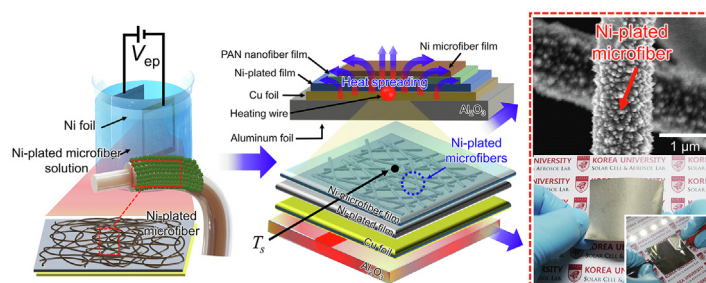
^c LG Electronics Inc., Seoul 06763, Republic of Korea

^d Department of Mechanical and Industrial Engineering, University of Illinois at Chicago, 842 W. Taylor Street, Chicago, Illinois 60607-7022, United States

HIGHLIGHTS

- Thin, flexible, wearable, heat-spreading, cooling films have been fabricated.
- The cooling films are decorated with highly nanotextured Ni microfibers.
- The Ni-electroplated microscale fibers could quickly spread heat over a solid medium.
- The cooling films could dissipate heat to the atmosphere via convective cooling.

GRAPHICAL ABSTRACT



ARTICLE INFO

Article history:

Received 10 March 2020

Received in revised form 15 June 2020

Accepted 5 July 2020

Available online 10 July 2020

Keywords:

Natural convection for air cooling

Heat spreading

Nickel microfibers

Electrospinning

Electroplating

ABSTRACT

Malfunctioning caused by hotspots in high-power and high-density microelectronics has been a major problem, particularly for miniaturized advanced portable electronic devices. The use of efficient heat spreaders or cooling films is a viable solution for mitigating the hotspot concern in high-power density electronic devices. In this study, we fabricated thin, flexible, wearable, heat-spreading cooling films decorated with highly nanotextured Ni microfibers. The Ni-electroplated microfibers could quickly spread heat over a solid medium and dissipate heat to the atmosphere via convective cooling. In the present parametric studies, the Ni electroplating time varied from 45 to 60 and 90 min. The optimal condition, which yielded the lowest thermal resistance and the highest heat transfer coefficient, was identified. The Ni microfibers were characterized using scanning electron microscopy, X-ray diffraction, and transmission electron microscopy analyses.

© 2020 Elsevier Ltd. All rights reserved.

1. Introduction

High-performance electronic chips are a constantly evolving technology for information technology (IT) applications, including cloud computing, artificial intelligence, and internet of things (Aitken et al., 2014; Alhawari et al., 2013; Hsieh et al., 2016;

Samie et al., 2016). Researchers in the IT industry have been working on developing faster chips that would be capable of processing and storing large amounts of data. Microchips have become critical tools for many IT applications, including industrial process automation, vehicles, electronic communications, equipment control, entertainment, and education (Falck et al., 2018; Wang et al., 2013). However, researchers working toward developing advanced processors still face challenges because of the increasingly stringent thermal management for high-power density or heat-flux electronics. The increasing demands for miniaturized

* Corresponding authors.

E-mail addresses: esan@skku.edu (S. An), ayarin@uic.edu (A.L. Yarin), skyoons@korea.ac.kr (S.S. Yoon).

¹ These authors have equally contributed.

electronics featuring excellent versatility and functionalities led to the fabrication of high-power density and high-heat flux devices, which pose great thermal-management challenges for the IT industry (Kadam and Kumar, 2014; Kheirabadi and Groulx, 2016; Sevinchan et al., 2018; Zhang et al., 2014).

The adequate cooling of the existing IT applications is achieved using classical thermal management systems, such as fan/heat sink and heat sink/heat pipe combinations (Bar-Cohen and Wang, 2009; Chowdhury et al., 2009; Greco et al., 2014; Majumdar, 2009; Rao et al., 2013; Wang and Bar-Cohen, 2007; Zuo et al., 2001). To alleviate the high-heat flux conditions, cooling systems must accommodate voluminous heat sinks and large fan systems. Such approaches pose two major problems. First, the device volume must increase, which is against the principle of miniaturized electronics. Second, the manufacturing cost of these bulky cooling systems are high and add to the financial burden of the manufacturers. Therefore, the thermal power management of emerging advanced electronics has become a three-fold complex problem because of the following reasons: (i) thermal resistance must be reduced; (ii) the size constraints of the IT applications are becoming increasingly stringent owing to the miniaturization-driven electronics market; (iii) and the additional environmental burden imposed by any newly developed cooling technologies must be minimized (Choi and Jeong, 2016; Morales-Fuentes and Loredó-Sáenz, 2018; Ong et al., 2017; Rao et al., 2016). For these reasons, the development of thin films of low thermal resistance, light-weighted, and large surface-to-volume ratio is required. There have been numerous studies to meet these stringent requirements (Fischer et al., 2017; Freystein et al., 2016; Jun et al., 2013; Patel et al., 2016; Sahu et al., 2015b, 2016; Sankaran and Yarin, 2018; Sankaran et al., 2018; Sinha-Ray et al., 2014; Sinha-Ray and Yarin, 2014; Sinha-Ray et al., 2017a; Sinha-Ray et al., 2017b; Staszal et al., 2019; Staszal and Yarin, 2018). Sinha-Ray et al. (2010) introduced various electroplated fibers and used them as a spray cooling mat. Sahu et al. (2015a) studied the hydrodynamic focusing effect by impacting drops into a porous filter film. Freystein et al. (2016) used nanofibers to enhance heat transfer in forced convective boiling of the mini-channel. Sahu et al. (2016) used extremely thin supersonically-blown nanofibers to increase the critical heat flux for pool boiling applications. Sinha-Ray (2017) demonstrated removal of heat in pool boiling from a heater mimicking high-power microelectronics that facilitated a swing motion of the heater. However, none of these studies has addressed the issues of lowering thermal resistance and heat spreading capability of the films for a concentrated heat source, namely a "hot spot".

Here, we aim to address these thermal concerns (in particular, thermal resistance and heat spreading) associated with advanced electronics by introducing thin, flexible, light-weighted heat-spreading/cooling films that could be easily attached to any surfaces. This approach based on the nanotexture material developed for this purpose is novel and holds great promise in a plethora of applications. In previous studies (Peacock et al., 2016; Shtein et al., 2015; Song et al., 2014; Xu et al., 2009; Yu et al., 2007; Zhang et al., 2018; Zhang et al., 2015), 1D or 2D materials such as carbon nanotubes, graphene, and silver nanowires have been used as efficient heat spreaders while taking advantage of their superior heat conductivities. Furthermore, these 1D and 2D materials provided roughened or textured surface, which increased the surface area and the corresponding convective cooling. Copper fibers of the 1D structure were also used as an efficient cooling mat (An et al., 2016). However, their heat spreading capability was not demonstrated, not to mention cooling and heat spreading capabilities of other types of metal fibers. This is one of the aims of the present work.

We developed highly nanotextured nickel-electroplated 1D microfibers via electroplating Ni on electrospun polymer nanofibers, which led to a significant increase in the surface area of the films. The effective heat transfer coefficient (h_{eff}) has been experimentally measured to estimate the cooling efficiency of the fabricated nanotextured films. Furthermore, electrospinning and electroplating are based on facile, scalable, and cost-effective processes, and therefore, these films hold great promise for developing the next-generation of thin and flexible microelectronic devices.

2. Experimental

2.1. Electroplating Cu substrate

The first step in the fabrication of the heat-spreading films was Ni electroplating (Fig. 1a). The Ni electroplating solution was prepared by mixing 80 g of nickel(II) sulfamate tetrahydrate (Sigma Aldrich, USA), 2 mL of single-distilled deionized (DI) water (Samchun Pure Chemical, Korea), and 6 g of boric acid (H_3BO_3 , 99.97%, Sigma Aldrich, USA). Then, the electroplating voltage of 3 V (the electric current of 3.4 A) was applied to a Cu foil ($5 \text{ cm} \times 5 \text{ cm}$) using a direct current (DC) power supply (E3644A, Agilent Tech, USA) for 3 min (Fig. 1a). The Ni-plated film was subsequently rinsed with formaldehyde (40%, Sigma Aldrich, USA) and DI water for 15 min and 10 s, respectively. The rinsed film was then dried for 10 min under Ar atmosphere.

2.2. Electrospinning nanofibers

First, an 8 wt% polyacrylonitrile (PAN, Sigma Aldrich, $M_w = 150,000 \text{ Da}$) solution dissolved in *N,N*-dimethylformamide (DMF, Reagent Duksan, South Korea) was prepared and used to fabricate an electrospun nonwoven PAN nanofiber mat. During electrospinning, PAN solution was supplied using a syringe pump (Legato 100, KD Scientific Inc., USA) and an 18-gauge needle (Nordson EFD, USA) at the flow rate of $300 \mu\text{L}\cdot\text{h}^{-1}$. Simultaneously, the high DC voltage of 6.5 kV was applied to the needle using the high DC voltage supply (E3644A, Agilent Tech, USA). The electrospun fibers were deposited onto the Ni-electroplated film ($5 \text{ cm} \times 5 \text{ cm}$) for 3 min (Fig. 1b).

2.3. Electroplating Ni microfiber film

A slightly different Ni-electroplating solution than that described in Section 2.1. was used to fabricate the Ni microfibers (An et al., 2014; Sinha-Ray et al., 2010). The solution was prepared by adding 8 g of nickel chloride hexahydrate (99.9%, Sigma Aldrich, USA) and 8 g of H_3BO_3 to DI water. The final volume of the as-mixed solution was set to 160 mL by adjusting the amount of DI water. Then, the as-mixed solution was magnetically stirred at 500 rpm at $60 \text{ }^\circ\text{C}$ for 30 min. Afterwards, 22 mL of HCl solution (2 mL HCl + 20 mL DI water; in this study we used 37% HCl) and 22 mL of NH_4OH solution (2 mL NH_4OH + 20 mL DI water) were added to the magnetically stirred solution in this order. The electrospun PAN nanofiber mat ($A_p = 5 \text{ cm} \times 5 \text{ cm}$; 25 cm^2) and Ni foil ($A_p = 5 \text{ cm} \times 5 \text{ cm}$; 25 cm^2) were positioned to face each other and then, simultaneously immersed in the Ni electroplating solution (Fig. 1c). Subsequently, the electric current density of $2 \text{ mA}\cdot\text{cm}^{-2}$ was applied to the specimens using the DC power supply. To vary the average diameter of the Ni microfibers, we used different electroplating times: 0, 45, 60, and 90 min, and the corresponding samples were denoted as Ni0, Ni45, Ni60, and Ni90, respectively. A photograph of the as-formed Ni microfiber film is presented in Fig. 1d, and a snapshot of an LED operated using the Ni microfiber

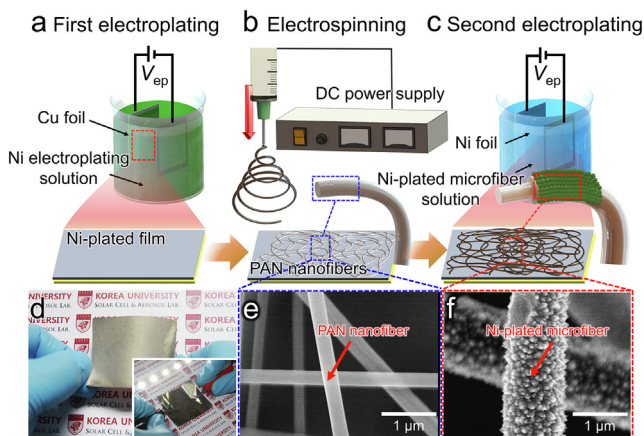


Fig. 1. Schematics of fabrication processes of (a) Ni-plated film, (b) electrospun polyacrylonitrile (PAN) nanofibers, and (c) Ni-plated microfibers, where V_{ep} denotes the electroplating voltage. (d) Photographs of Ni microfiber film and snapshot of LED operated using the film in the inset. Scanning electron microscopy images of (e) bare PAN nanofibers and (f) Ni microfibers.

film is illustrated in the inset. This demonstrated the high conductivity of the nanofiber film, which was comparable to that of commercial electric wires. The scanning electron microscopy (SEM) images of the PAN nanofibers and Ni microfibers (Fig. 1e and f) illustrate that the diameter of the Ni-plated fibers significantly increased after Ni-electroplating. It should be emphasized that the surface of the Ni-plated fibers was highly textured.

2.4. Heat transfer evaluation

When the heat transfer performance of the heat spreading films was evaluated, a Ni-Cr wire (the resistance of $5.73 \Omega \cdot \text{m}^{-1}$, diameter of 1 mm, and 5 cm long) was placed between the Al_2O_3 substrate and the heat-spreading film, and was used as a line heat source (Fig. 2). Joule heating was applied to the Ni-Cr wire by connecting it to a DC power supplier. The electric power of $q_{exp} = 0.160, 0.169, 0.187, 0.196, 0.202, 0.214, 0.223,$ and 0.24 W was supplied to heat the Ni-Cr wire. The supplied current (I) and voltage (V) were measured by a Clamp-On AC/DC HiTester (HIOKI 3288, HIOKI, JAPAN) and a Digital multimeter (HIOKI DT4212, HIOKI, JAPAN), respectively. The total electrical heating power was $q_{exp} = I \cdot V$. The Al_2O_3 substrate (the thermal conductivity of $25\text{--}30 \text{ W} \cdot \text{m} \cdot \text{K}^{-1}$) was used as an insulator to minimize the heat losses outside the tested box, while the Al_2O_3 substrate was encased with a glass fiber insulator, as illustrated in Fig. 2. The acrylic box ($50 \text{ cm} \times 50 \text{ cm} \times 20 \text{ cm}$) was used as a holder for the fabricated film, the Al_2O_3 substrate, and the glass fiber; see Fig. 2. The purpose of the box was to provide stable inflow and outflow for accurate measurements of T_s . The box had an open top although the top was partly covered with an aluminum (Al) foil with many holes, which escaped the rising air. There was a sufficiently large gap (10 cm) between the Al foil and the box holder, which permitted an entrained air inflow and facilitated a buoyancy-driven flow in the region. The surface temperature of the heat spreaders, T_s , and the constant atmospheric temperature inside the box, $T_\infty = 20 \text{ }^\circ\text{C}$, were measured and recorded using a K-type thermocouple (probe size of $1 \text{ mm} \times 150 \text{ mm}$ and uncertainty range of $\pm 0.5 \text{ }^\circ\text{C}$) and a data logger (GL-240, Graphtec, USA), respectively.

2.5. Characterization of heat spreading films

An atomic force microscopy (AFM; XE-100, Park Systems) instrument operated in non-contact mode and a high-resolution

scanning electron microscopy (HR-SEM; XL30 SFEQ, Phillips Co., Netherlands) device operated at 15 kV were used to measure the roughness and explore the surface morphology of the heat spreaders, respectively. The crystallinity of the Ni microfibers was investigated using an X-ray diffraction (XRD; SmartLab, Rigaku) system. A transmission electron microscopy (TEM; JEM 2100F, JEOL, Inc.) instrument equipped with an energy-dispersive X-ray spectroscopy (EDS) system was used to examine the surface morphology and elemental distributions of the Ni microfibers, respectively.

An infrared (IR) camera (FLIR-E63900, FLIR System, Inc.) was used to observe the heat transfer on the heat spreaders; the heat sensitivity and error range of the camera were 30 mK at $25 \text{ }^\circ\text{C}$ and approximately 1%, respectively. Prior to the experiments, the temperature of an object was determined using a thermocouple, and the IR camera was calibrated using this measured temperature value to ensure the accurate reading of the IR camera's output. The emissivity of the IR camera of $\epsilon = 1$ produced the correct readings which are in agreement with the thermocouple measurements. The IR camera temperature reading automatically also accounted for heat transfer by radiation although the radiation effect is minimal because the highest temperature was less than $150 \text{ }^\circ\text{C}$.

3. Results and discussion

3.1. Characterization of the films

The purpose of the X-ray diffraction (XRD) or transmission electron microscopy (TEM) measurements is to confirm the presence of carbon and nickel in the electroplated film. The XRD patterns of the Ni-plated microfibers and bare Cu foil are depicted in Fig. 3a. The XRD peaks in the 2θ range of $20^\circ\text{--}80^\circ$ were explored (the scanning resolution of 0.01), and sharp peaks that confirmed the crystallinity of the Ni-plated fibers were observed. In detail, the peaks at $2\theta = 45^\circ, 50^\circ$ and 76° in the XRD spectrum of the Ni microfibers corresponded to the (111), (200), and (220) planes, respectively, of pure Ni (JCPDS 04-0850). The peaks in the XRD profile of the bare Cu foil at $2\theta = 42^\circ, 50^\circ,$ and 74° corresponded to the (111), (200), and (220) planes, respectively, of pure Cu (JCPDS 04-0836). Fig. 3b illustrates the high-magnification TEM image of a single Ni microfiber that was fabricated using the electroplating time of 60 min, where the d -spacing of 0.202 nm corresponded to the (111) plane of elemental Ni (Du et al., 2004). This finding was in good agreement with the XRD results (Fig. 3a). The elemental mapping images of the Ni microfibers (Fig. 3d and 3e) revealed the presence of the C (core) and Ni (shell) in their structure, and thus, demonstrated that Ni shall be well-formed on the surface of the polyacrylonitrile (PAN) nanofibers.

3.2. Thermal resistance and heat spreading capability of the films

The cooling performance of the films was investigated by applying constant electric heating power and measuring the corresponding surface temperature of the film as a function of time. The textured surface should decrease the temperature T_s because of an increased surface area, which is equivalent to increasing the effective heat transfer coefficient (h_{eff}); $q_{exp} = h_{eff} A_p \Delta T$. Because $R_{th} = \Delta T / q_{exp}$, R_{th} can be estimated when ΔT and q_{exp} are measured. Then, h_{eff} is estimated as $h_{eff} = 1 / (R_{th} A_p)$.

Fig. 4a illustrates the changes in the excess temperature $T_s - T_\infty$. In Fig. 4a, the legends low, med, and high correspond to $q_{exp} = 0.16, 0.187,$ and 0.202 W . As heating progressed, the values of $T_s - T_\infty$ saturated and eventually reached constant levels after 1200 s (Fig. 4a). At $q_{exp} = 0.16 \text{ W}$, the steady-state values of $T_s - T_\infty$ of the bare PAN nanofibers and Ni microfiber films were 17.4 and $14.0 \text{ }^\circ\text{C}$, respectively. At $q_{exp} = 0.187 \text{ W}$, the steady-state values

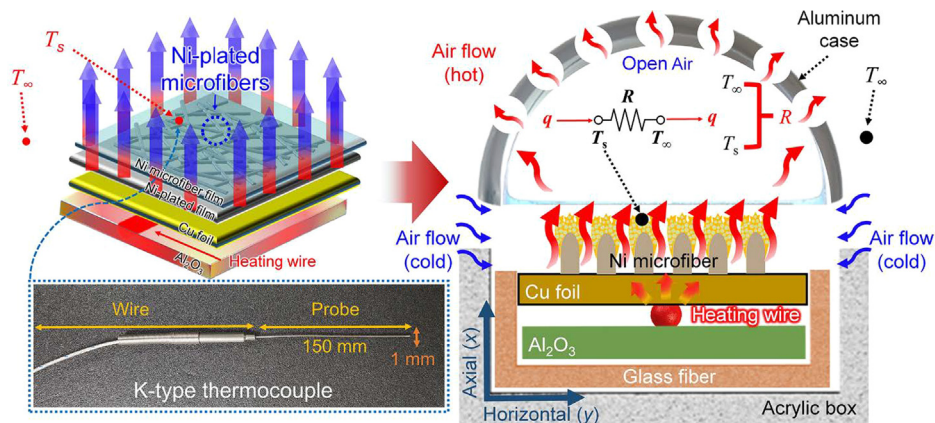


Fig. 2. Schematics of bare PAN nanofiber and Ni microfiber films used for natural convection air cooling and heat spreading tests. The surface temperature, T_s , measured at the specimen center as noted.

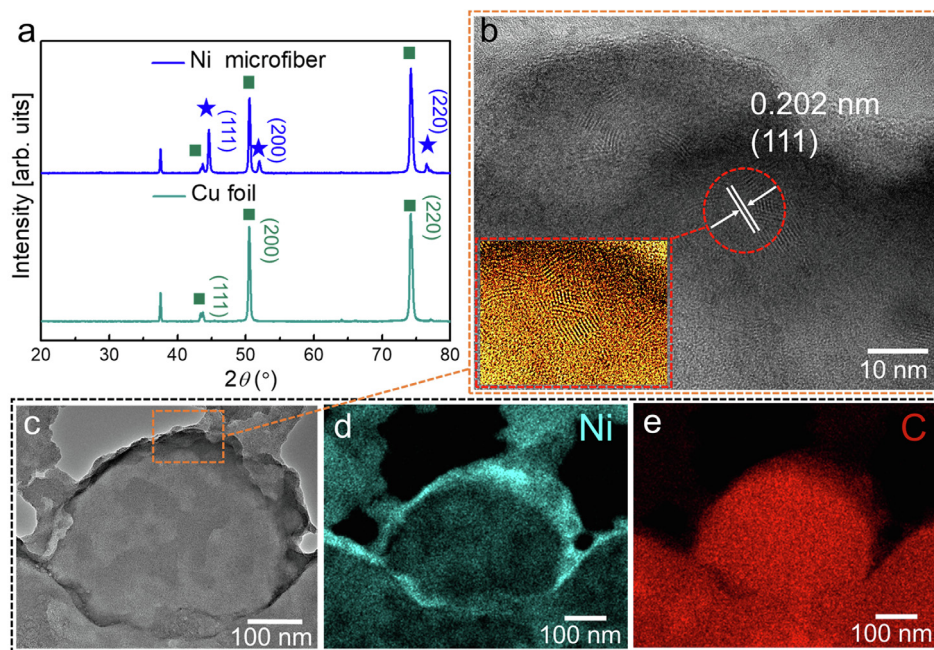


Fig. 3. (a) XRD patterns of Ni microfibers and bare Cu foil. (b) The high-magnification TEM image of the Ni microfiber. (c) Cross-sectional TEM image of single Ni microfiber. (d) and (e) Elemental mapping images of the Ni microfiber.

of $T_s - T_\infty$ of the PAN nanofibers and Ni microfiber films reached at 34.0 and 28.9 °C, respectively. At $q_{\text{exp}} = 0.202$ W, the steady state $T_s - T_\infty$ values of the PAN nanofiber and Ni microfiber films were 49 and 41 °C, respectively. Therefore, the difference in the values of $T_s - T_\infty$ of the PAN nanofibers and Ni microfiber films increased from 3 to 5 and to 8 °C as q_{exp} increased from 0.16 to 0.187 and to 0.202 W, respectively (Fig. 4a). This pattern indicated that the heat removal by natural convection was enhanced by using the Ni microfibers (An et al., 2016; An et al., 2014; Sinha-Ray et al., 2010)

Fig. 4b illustrates the changes in thermal resistance, R_{th} , as a function of q_{exp} (Kim et al., 2019). The thermal resistance is defined as $R_{\text{th}} = (T_s - T_\infty)/q_{\text{exp}}$. A low T_s value would imply low thermal resistance and hence efficient air cooling at given q_{exp} . The values of R_{th} of the Ni microfiber films are lower than those of the bare PAN nanofiber film for the entire range of q_{exp} . This lower R_{th} was attributed to an increase in the surface area of the highly nano-textured surface of the Ni-plated fibers. This implies that the Ni microfiber film revealed a stronger cooling by natural convection

than the bare PAN nanofiber film (Hu and Chung, 2011; Lin and Chung, 2009; Shahil and Balandin, 2012).

The infrared (IR) images of the Ni microfiber films were obtained to evaluate their heat spreading capability. The time evolution of the heat spreading for the bare PAN nanofiber film is illustrated in Fig. 4c, where an apparent hotspot is concentrated in the middle of the substrate. On the other hand, Fig. 4d depicts the efficient heat spreading over the Ni60 film. It should be reminded that the Ni-Cr heating wire used to apply heat was sandwiched between the insulating Al_2O_3 substrate and Ni microfiber film. The IR images were obtained for 600 s when $q_{\text{exp}} = 0.202$ W was applied to the Ni-Cr heating wire. Overall, the surface temperature recorded in the IR images gradually increased over time although the pattern of heat spreading for the PAN and Ni60 films is different.

For the PAN nanofiber film, the heat from the hotspot was not efficiently removed toward the edges of the film, which resulted in the center area being intensively heated because of insufficient

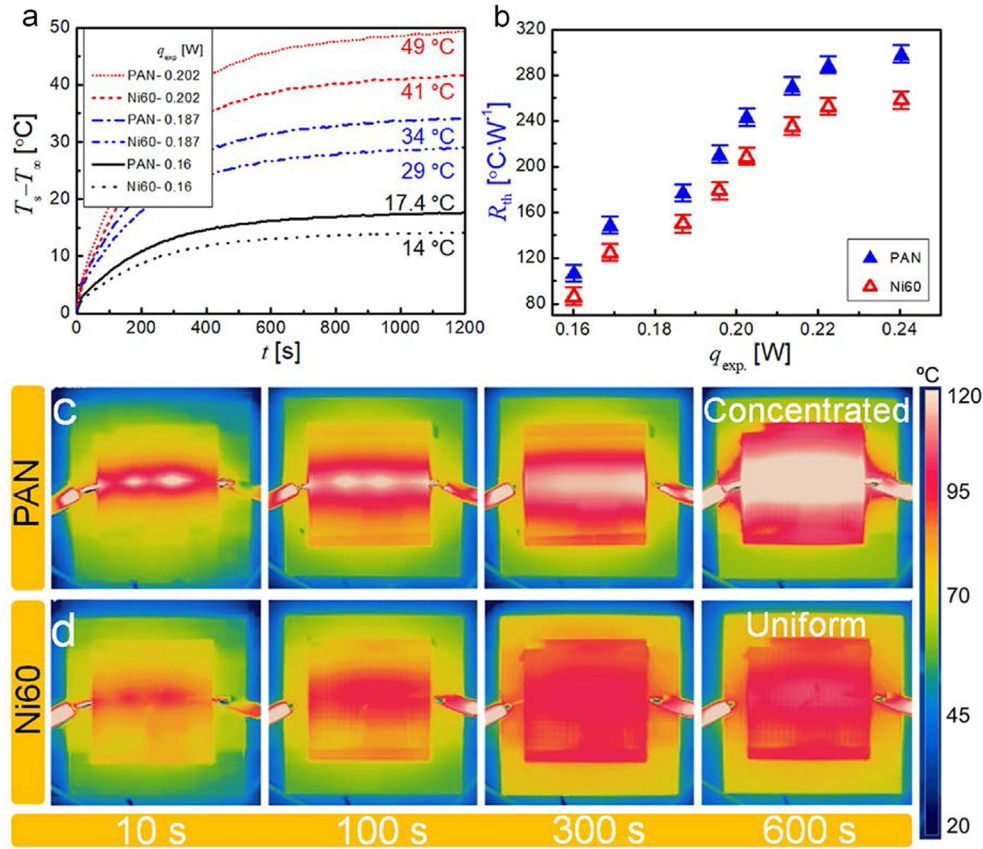


Fig. 4. (a) Time-dependent excess temperature $T_s - T_\infty$ when heating power, $q_{exp} = 0.16, 0.187,$ and 0.202 W. (b) Thermal resistance (R_{th}) of PAN nanofibers (\blacktriangle) and Ni microfiber films (\triangle) as function of q_{exp} . IR images of (c) PAN nanofibers and (d) Ni microfiber films at $q_{exp} = 0.202$ W.

heat spreading. By contrast, for the Ni60 film the heat from the hot-spot was evenly and effectively diffused throughout the entire area of the film. Therefore, in addition to the enhanced natural convection air cooling, the Ni-plated fiber film reveals an enhanced heat spreading performance owing to the presence of thermally conductive Ni metal.

3.3. Optimal film for heat removal via convection cooling

Fig. 5a–5d illustrate the scanning electron microscopy (SEM) images of the Ni0, Ni45, Ni60 and Ni90 films. The average diameter of the bare PAN nanofibers was 0.35 ± 0.03 μm and their roughness measured using the atomic force microscopy (AFM) was 0.23 μm . The average diameter increased to 3.4 ± 0.07 μm as the electroplating time increased to 90 min, and the roughness decreased to 0.83 and 0.38 μm at the electroplating times of 60 and 90 min, respectively. The roughness values of the Ni45 and Ni60 films were larger than those of the bare PAN nanofiber film, and thus led to a decrease in the value of R_{th} of the Ni45 films. However, when the Ni electroplating time exceeded 60 min, the diameter of the fibers and thickness of the overall film increased, that decreased the roughness and increased thermal insulating ability of the film (Kim et al., 2019). Hence, the surface area reduced and cooling capability decreased.

The cross-sectional SEM images of the PAN nanofibers deposited on Cu foil are presented in the third column of Fig. 5a. The cross-sectional images of the Ni microfibers deposited on Cu foil obtained after 45, 60, and 90 min of electroplating are illustrated in Fig. 5b, 5c, and 5d, respectively. When the electroplating time was 45 min, the thickness of the layer deposited on the Cu foil

was 2 μm and it increased up to 2.6 and 4 μm as the electroplating time increased to 60 and 90 min, respectively.

The inset in Fig. 5f sketches the electrical circuit scheme associated with the convective cooling by natural convection. As described in Fig. 2, the heat from the Al_2O_3 substrate was practically isotropically transferred because the Ni-Cr wire was placed at the center of the specimens. To simplify the analysis, in this study, we employ the one-dimensional analysis in the calculation of the heating power from the surface at the temperature T_s to air at T_∞ . The bottom surface of the Al_2O_3 substrate was well insulated with glass fibers, and thus, no heat loss through the bottom surface was assumed. Moreover, it was assumed that the radiative heat loss was negligible because $T_s < 100$ °C (Elliott, 1960; Kim et al., 2019; Kutscher et al., 1993). Accordingly, the only heat loss occurred through the top surface of the cooling film via natural convection, and was estimated using the equation $q_{exp} \sim h_{eff} A_p (T_s - T_\infty)$, where h_{eff} is the effective convective heat transfer coefficient and A_p is the projected area of the film. Thus, the h_{eff} could be expressed in terms of thermal resistance R_{th} as follows:

$$R_{th} = \frac{T_s - T_\infty}{q_{exp}} = \frac{1}{h_{eff} A_p} \quad (1)$$

Fig. 5f presents the values of R_{th} , which were associated with the natural convective cooling that occurred at the surface of films, as a function of the electroplating time (i.e., 0, 45, 60, and 90 min). The values of R_{th} in Fig. 5f were obtained at $q_{exp} = 0.202$ W. The values of R_{th} for the Ni0, Ni45, Ni60, and Ni90 films were 243, 220, 208, and 226 °C·W⁻¹, respectively. The values of R_{th} of the films decreased as the electroplating time increased, except for the Ni90 film. Moreover, the Ni60 film revealed the lowest value of

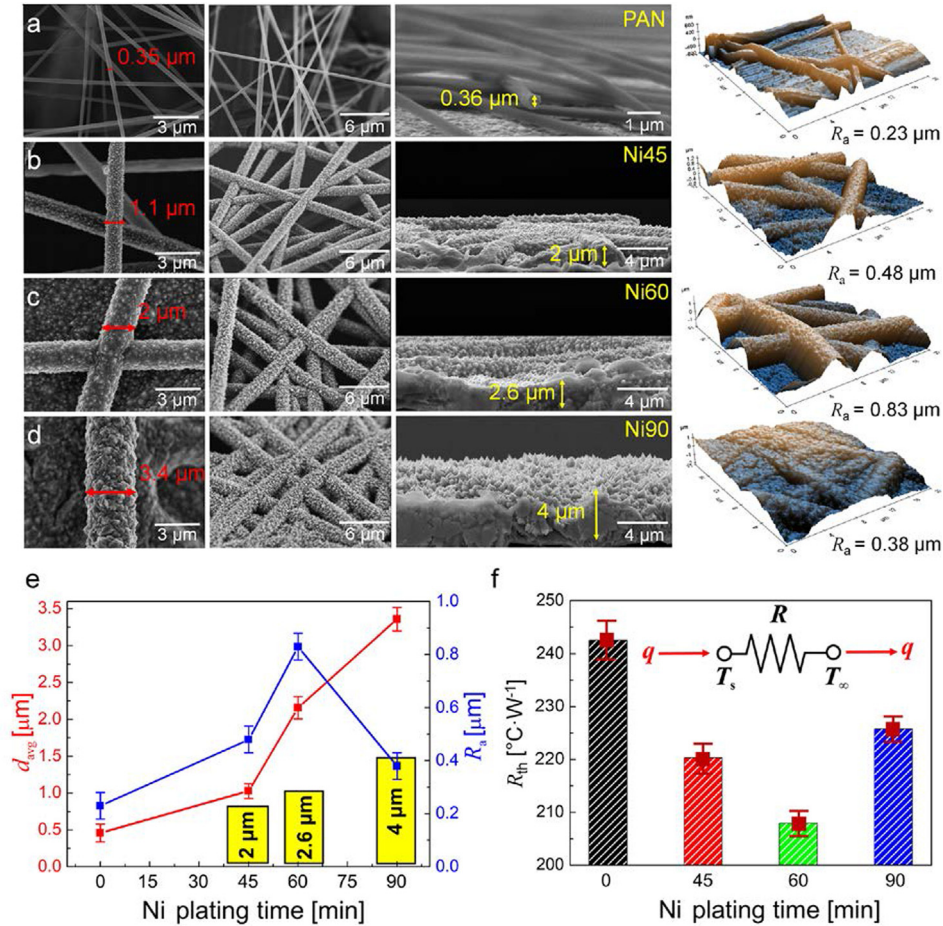


Fig. 5. SEM and AFM images of (a) bare PAN nanofibers and Ni microfiber films obtained after different electroplating times: (b) 45, (c) 60, and (d) 90 min. (e) The corresponding average fiber diameter (d_{avg} , the red line), average roughness (R_a , the blue line), and thickness (the yellow bars) of Ni microfiber films. (f) Thermal resistance (R_{th}) of films obtained at different electroplating times (Ni0, Ni45, Ni60, and Ni90) at $q_{exp} = 0.202$ W.

R_{th} . The increase in R_{th} of the Ni90 film was attributed to the reduced surface area and an increase in the film thickness, facilitating thermal insulation instead of boosting the natural convective air cooling. Thus, it can be concluded that the electroplating time of 60 min was the most optimal one, because the Ni60 film revealed the best natural convective cooling performance.

Table 1 compares the convective heat transfer coefficient, h_{eff} , of the films obtained using various electroplating conditions at $q_{exp} = 0.202$ W; the values of h_{eff} were obtained using Newton's law of cooling:

$$h_{eff} = \frac{q}{A_p(T_s - T_{\infty})} \quad (2)$$

The removed heat, q , is empirically estimated to compare its value against the previously measured supplied heat of q_{exp} (An et al., 2016; Kim et al., 2019):

$$q = h_b A_w (T_s - T_{\infty}) \quad (3)$$

where h_b is the heat transfer coefficient of air with respect to the Ni-electroplated Cu film in the absence of PAN fibers and texturing, and A_w is the surface area of the heating wire, where $A_w = \pi dL$, where d and L are the diameter ($d = 1$ mm) and length of the wire ($L = 0.05$ m), respectively. The values of the temperature T_s of the bare Cu foil and the Ni-electroplated Cu foil (i.e., bare Ni-plated surface) were essentially the same because these foils were subjected to the same heating power, in spite their thickness being slightly different. For example, if q , h_{eff} , and A_p of different films were the

same, the values of the excess temperature ($T_s - T_{\infty}$) of the films should be the same. Here T_s and T_{∞} are the surface temperature of the heated bare Ni-plated Cu film and the ambient temperature, which were 77.1 and 28 °C, respectively. In addition, h_b was obtained using the Nusselt number, Nu : $h_b = Nu \cdot k/d$, where k is the thermal conductivity of air. Furthermore, k was determined to be 0.0286 W·m⁻¹·K⁻¹ using the so-called film temperature, T_f , where $T_f = (T_s + T_{\infty})/2 = 52.55$ °C. For natural convection of air from a horizontal cylinder (heating wire) the Nu can be calculated using the Grashof (Gr) and Prandtl (Pr) numbers, as follows (Kim et al., 2019):

$$GrPr = g\beta(T_s - T_{\infty})d^3Pr/\nu^2 \quad (4)$$

and

$$Nu = 1.02 \cdot (GrPr)^{0.148} \quad (5)$$

where g is the gravity acceleration (9.81 m·s⁻²), β is the thermal expansion coefficient of air, which is defined as $\beta = T_f^{-1} = 0.00307$ K⁻¹, and ν is the kinematic viscosity of air at T_f . Here, $Pr = 0.7228$ and $\nu = 0.00001798$ m²·s⁻¹ (An et al., 2016). When h_b , A_w , and $(T_s - T_{\infty})$ are known, q could be calculated using Eq. (3), and in the present case it was found as $q = 0.266$ W. The values of h_{eff} , which were subsequently calculated using Eq. (2), are listed in Table 1. It should be noted that the empirical $q = 0.266$ W and the measured $q_{exp} = 0.202$ -W differ by ~24%. This comparison confirms the reasonable accuracy of the empirical prediction.

Table 1

Convective heat transfer coefficients, h_{eff} , of films as a function of Ni electroplating time at $A_p = 0.0025 \text{ m}^2$ and $q_{\text{exp}} = 0.202 \text{ W}$, which corresponds to $q = 0.266 \text{ W}$. All values here were computed using the empirically estimated power, q .

Film	h_{eff} [$\text{W}\cdot\text{m}^{-2}\cdot\text{K}^{-1}$]	Δh_{eff} with respect to $h_{\text{eff, Cu foil}}$ [%]	h_{eff}^{-1} or $R_{\text{th}}A_p$ [$\text{m}^2\cdot\text{K}\cdot\text{W}^{-1}$]	R_{th} [$\text{K}\cdot\text{W}^{-1}$]
Bare Cu foil (w/o fibers)	2.14	–	0.467	187
Ni-plated Cu foil (w/o fibers)	2.14	–	0.467	187
Ni0 (w/ PAN fibers only)	2.16	1	0.463	185
Ni45	2.39	12	0.418	167
Ni60	2.53	18	0.395	158
Ni90	2.33	9	0.395	172

For the bare PAN nanofiber film, $h_{\text{eff}} = 2.16 \text{ W}\cdot\text{m}^{-2}\cdot\text{K}^{-1}$, which was similar to the values of h_{eff} of the bare Cu foil or/and Ni-electroplated Cu foil ($2.14 \text{ W}\cdot\text{m}^{-2}\cdot\text{K}^{-1}$) (Table 1). The negligible difference in the values of h_{eff} implies that the PAN nanofibers had no positive effect on heat transfer or cooling.

As the electroplating time of Ni microfiber films increased from 45 to 60 min, h_{eff} gradually increased from 2.39 to $2.53 \text{ W}\cdot\text{m}^{-2}\cdot\text{K}^{-1}$, which indicated that cooling of the surface was enhanced (which lowered T_s). However, the value of h_{eff} of the Ni90 film decreased to $2.33 \text{ W}\cdot\text{m}^{-2}\cdot\text{K}^{-1}$. The excessive Ni electroplating filled all the gaps between the PAN fibers (Fig. 5d), which reduced surface texture, as is quantitatively indicated by the roughness of the films (Fig. 5e), and thus, reduced or even completely blocked the hydrodynamic focusing effect discussed above (Lembach et al., 2010; Sinha-Ray et al., 2014; Sinha-Ray and Yarin, 2014; Weickgenannt et al., 2011; Yarin et al., 2017). These results confirmed that excessive deposition of Ni reduced the cooling effect, and consequently the optimal texturing was achieved at the intermediate electroplating time of 60 min.

The h_{eff} value of the bare Cu foil is $h_{\text{eff}} = 2.14 \text{ W}\cdot\text{m}^{-2}\cdot\text{K}^{-1}$. The h_{eff} value of the Ni45 film is approximately 12% higher than that of the bare Cu film. Furthermore, the h_{eff} value of the Ni60 film is 18% higher than that of the bare Cu foil. This is a significant improvement that enables us to control the surface temperature between 10 and 40 °C. This flexibility in temperature control leaves plenty of room for improvement of the hotspot-induced malfunctions for portable electronic devices.

Fig. 6a presents the results of the spray cooling test for the Ni0, Ni45, Ni60, and Ni90 films. In these tests, the film surface temperature T_s was 130 °C, as measured using a probe thermometer. Initially, the value of T_s of the films was approximately the same as the temperature of the hot plate below, but it gradually decreased over time when water droplets were sprayed on the surfaces of the films. Spraying was repeated approximately 13 times, and the value of T_s sharply decreased every time water droplets hit the surfaces of the films and evaporated. Accordingly, the latent heat of water evaporation absorbed heat from the surface and thus, removed it. Once all the water droplets evaporated, the value of T_s increased again and the pattern was repeats 13 times until $t = 420 \text{ s}$. The practically instantaneous decrease in the temperature T_s was significant and ranged from 30 to 40 °C. The most important factor that contributed to the rapid evaporation of water droplets was the surface roughness of the films. Wettability plays an important role in spreading the droplets and promotes or hinders the evaporation process. When the surface is highly wettable (or hydrophilic), the droplet spreading is enhanced, and a thin liquid film, which is easier to evaporate, forms. Accordingly, the practically instantaneous heat removal is facilitated in such cases.

To investigate the wettability of the films we measured their static contact angles, and the results are presented in Fig. 6b. The water contact angle on the Ni0 film was 58°. As the Ni-electroplating time increased, the hydrophilicity of the film surface

increased, although the difference between the hydrophilicities of the Ni60 and Ni90 films appeared to be negligible.

Fig. 6c illustrates the results of the dynamic wettability test of the four films for 3 s. All released droplets had a diameter of $D_0 = 3 \text{ mm}$. They were released from the height of $H = 18 \text{ cm}$. The liquid spreading motion has practically ceased at $\sim 30 \text{ ms}$. The impacting droplets spread and form edge rims at the periphery, which result in the radial fingers. Once the spreading droplets reach the maximum diameter, they receded and thickened back, which was observed in the images of the Ni0, Ni45, and Ni60 films. The receding motion was reduced as the electroplating time increased. Eventually no receding motion was observed for the Ni90 film because the entire spreading liquid was imbibed in the film. The Ni90 film was the thickest ($4 \mu\text{m}$; Fig. 5d), and therefore, it was able to imbibe the largest amount of liquid. The images in Fig. 6c confirmed that the Ni90 film imbibed the spreading liquid, which prevented the receding of the liquid. Therefore, the Ni90 film appeared to be the most hydrophilic of all Ni films under both static and dynamic conditions, as demonstrated by the images in Fig. 6b and c, respectively. It should be emphasized that the film roughness changes result in a lower contact angle predicted by the formula for the Wenzel state, which facilitates capturing and holding recoiling water. Hydrodynamic focusing effect, which accompanies impact of macroscopic drops onto microscopic pores in the fiber mats also contributes significantly to prevention of receding motion and drop bouncing (Lembach et al., 2010; Sinha-Ray et al., 2014; Sinha-Ray and Yarin, 2014; Weickgenannt et al., 2011; Yarin et al., 2017). The hydrodynamic focusing effect was demonstrated experimentally and theoretically explained in (Lembach et al., 2010; Sahu et al., 2015a; Weickgenannt et al., 2011; Yarin et al., 2017) and it takes place on both pure polymer or metallized fiber mats, as well as any other types of fibrous mats with microscopic inter-fiber pores irrespective of fiber wettability. This type of dynamic imbibition happens even on superhydrophobic fibers, with water drops easily penetrating into, for example, Teflon fiber mats, etc. (Lembach et al., 2010; Sahu et al., 2015a; Sinha-Ray et al., 2014; Sinha-Ray and Yarin, 2014; Weickgenannt et al., 2011; Yarin et al., 2017).

This type of change in wettability facilitates various heat transfer phenomena, as illustrated quantitatively in Fig. 6a. As the nanofiber films became more hydrophilic, the sprayed droplets adhered to the heated surface more efficiently and the heat transfer between the spreading droplets and heated surface was increased. This pattern was observed for the Ni0, Ni45, and Ni60 films; however, for the most hydrophilic film (Ni90), the pattern was reversed and droplet evaporation was, in fact, hindered, which led to an increase in T_s . Therefore, it was concluded that the Ni60 film presented the optimal thickness that facilitated the maximum heat transfer (or droplet evaporation). The smaller roughness of the Ni90 film compared with that of the Ni60 film also contributed to a decrease in the heat transfer because the contact surface area between the Ni fibers and water droplets was also reduced.

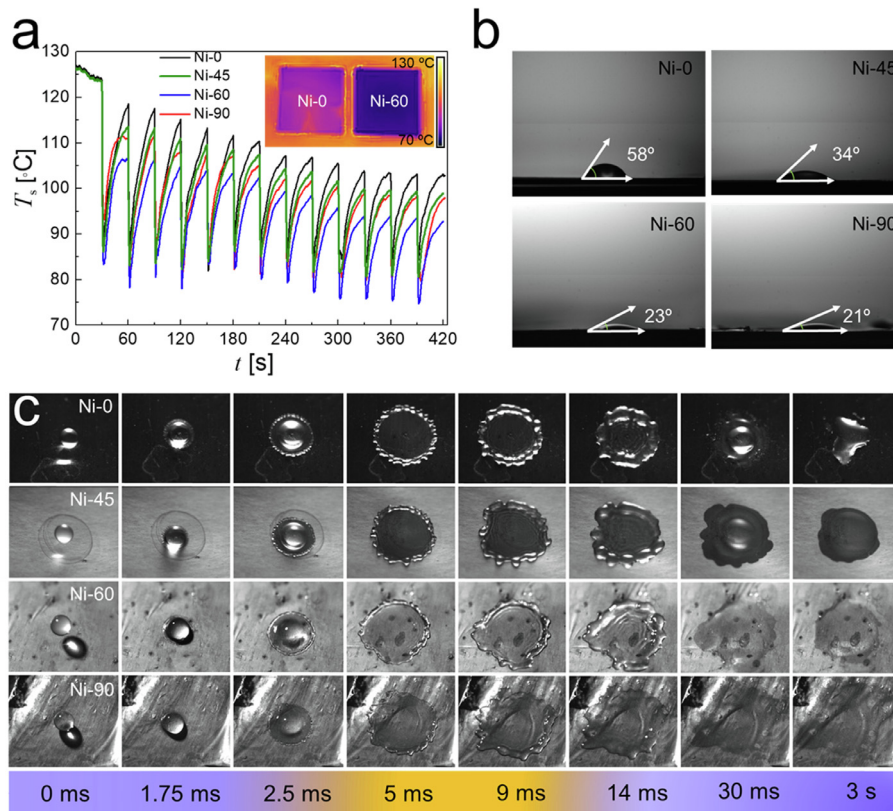


Fig. 6. (a) Changes in the surface temperature (T_s) during spray cooling of various films at the initial $T_s = 130$ °C. (b) Water contact angle with various films at 28 °C. (c) Drop impact phenomena on Ni0, Ni45, Ni60, and Ni90 films (in order from top to bottom) at $T_s = 130$ °C.

4. Conclusion

A method that combined electrospinning and electroplating was used to fabricate Ni-electroplated microfibers. The surface roughness of the individual Ni microfibers was high, which enabled them to achieve high performance during heat spreading and natural convection air cooling tests. In particular, the Ni60 film exhibited the highest performance compared with those of the Ni0, Ni45, and Ni90 ones. The use of the Ni microfiber films developed in the present study for future thin and flexible microelectronic devices is expected to address their hotspot problems by providing efficient heat removal and spreading.

Declaration of Competing Interest

The authors declare that they have no known competing financial interests or personal relationships that could have appeared to influence the work reported in this paper.

Acknowledgements

This work was supported by the National Research Foundation of Korea (NRF) grant funded by the Korea government (MSIT), NRF-2020R1A5A1018153. This research was also supported by the Technology Development Program to Solve Climate Changes of the National Research Foundation (NRF) funded by the Ministry of Science, ICT & Future Planning (NRF-2016M1A2A2936760).

References

Aitken, R., Chandra, V., Myers, J., Sandhu, B., Shifren, L., Yeric, G., 2014. Device and technology implications of the Internet of Things, 2014 Symposium on VLSI Technology (VLSI-Technology): Digest of Technical Papers. IEEE, 1–4.

- Alhawari, M., Mohammad, B., Saleh, H., Ismail, M., 2013. In: A survey of thermal energy harvesting techniques and interface. IEEE, pp. 381–384.
- An, S., Jo, H.S., Al-Deyab, S.S., Yarin, A.L., Yoon, S.S., 2016. Nano-textured copper oxide nanofibers for efficient air cooling. *J. Appl. Phys.* 119, 065306.
- An, S., Lee, C., Liou, M., Jo, H.S., Park, J.-J., Yarin, A.L., Yoon, S.S., 2014. Supersonically blown ultrathin thorny devil nanofibers for efficient air cooling. *ACS Appl. Mater. Interfaces* 6, 13657–13666.
- Bar-Cohen, A., Wang, P., 2009. On-chip hot spot remediation with miniaturized thermoelectric coolers. *Microgravity Sci. Technol.* 21, 351–359.
- Choi, J., Jeong, M., 2016. Compact, lightweight, and highly efficient circular heat sink design for high-end PCs. *Appl. Therm. Eng.* 92, 162–171.
- Chowdhury, I., Prasher, R., Lofgreen, K., Chrysler, G., Narasimhan, S., Mahajan, R., Koester, D., Alley, R., Venkatasubramanian, R., 2009. On-chip cooling by superlattice-based thin-film thermoelectrics. *Nat. Nanotechnol.* 4, 235.
- Du, Y., Chen, H., Chen, R., Xu, N., 2004. Synthesis of p-aminophenol from p-nitrophenol over nano-sized nickel catalysts. *Appl. Catal. A* 277, 259–264.
- Elliott, L., 1960. Similarity methods in radiation hydrodynamics. *Proc. R. Soc. London. Ser. A* 258, 287–301.
- Falck, J., Felgemaier, C., Rojko, A., Liserre, M., Zacharias, P., 2018. Reliability of power electronic systems: An industry perspective. *IEEE Ind. Electr. Magazine* 12, 24–35.
- Fischer, S., Sahu, R.P., Sinha-Ray, S., Yarin, A.L., Gambaryan-Roisman, T., Stephan, P., 2017. Effect of nano-textured heater surfaces on evaporation at a single meniscus. *Int. J. Heat Mass Transfer* 108, 2444–2450.
- Freystein, M., Kolberg, F., Spiegel, L., Sinha-Ray, S., Sahu, R.P., Yarin, A.L., Gambaryan-Roisman, T., Stephan, P., 2016. Trains of Taylor bubbles over hot nano-textured mini-channel surface. *Int. J. Heat Mass Transfer* 93, 827–833.
- Greco, A., Cao, D., Jiang, X., Yang, H., 2014. A theoretical and computational study of lithium-ion battery thermal management for electric vehicles using heat pipes. *J. Power Sources* 257, 344–355.
- Hsieh, Y.-T., Fang, C.-L., Su, C.-F., Tsai, H.-H., Juang, Y.-Z., 2016. In: A hybrid ambient energy harvesting integrated chip (IC) for the internet of things (IoT) and portable. IEEE, pp. 1–4.
- Hu, K., Chung, D., 2011. Flexible graphite modified by carbon black paste for use as a thermal interface material. *Carbon* 49, 1075–1086.
- Jun, S., Sinha-Ray, S., Yarin, A.L., 2013. Pool boiling on nano-textured surfaces. *Int. J. Heat Mass Transfer* 62, 99–111.
- Kadam, S.T., Kumar, R., 2014. Twenty first century cooling solution: Microchannel heat sinks. *Int. J. Therm. Sci.* 85, 73–92.
- Kheirabadi, A.C., Groulx, D., 2016. Cooling of server electronics: A design review of existing technology. *Appl. Therm. Eng.* 105, 622–638.

- Kim, T.-G., Park, C.-W., Woo, D.-Y., Yoon, S.S., 2019. Efficient heat spreader using supersonically sprayed graphene and silver nanowire. *Appl. Therm. Eng.* 114572.
- Kutscher, C.F., Christensen, C.B., Barker, G.M., 1993. Unglazed transpired solar collectors: heat loss theory.
- Lembach, A.N., Tan, H.-B., Roisman, I.V., Gambaryan-Roisman, T., Zhang, Y., Tropea, C., Yarin, A.L., 2010. Drop impact, spreading, splashing, and penetration into electrospun nanofiber mats. *Langmuir* 26, 9516–9523.
- Lin, C., Chung, D., 2009. Graphite nanoplatelet pastes vs. carbon black pastes as thermal interface materials. *Carbon* 47, 295–305.
- Majumdar, A., 2009. Thermoelectric devices: helping chips to keep their cool. *Nat. Nanotechnol.* 4, 214.
- Morales-Fuentes, A., Loredó-Sáenz, Y., 2018. Identifying the geometry parameters and fin type that lead to enhanced performance in tube-and-fin geometries. *Appl. Therm. Eng.* 131, 793–805.
- Ong, K., Tan, C., Lai, K., Tan, K., 2017. Heat spreading and heat transfer coefficient with fin heat sink. *Appl. Therm. Eng.* 112, 1638–1647.
- Patel, V.K., Seyed-Yagoobi, J., Sinha-Ray, S., Sinha-Ray, S., Yarin, A.L., 2016. Electrohydrodynamic conduction pumping-driven liquid film flow boiling on bare and nanofiber-enhanced surfaces. *J. Heat Transfer* 138.
- Peacock, M.A., Roy, C.K., Hamilton, M.C., Johnson, R.W., Knight, R.W., Harris, D.K., 2016. Characterization of transferred vertically aligned carbon nanotubes arrays as thermal interface materials. *Int. J. Heat Mass Transfer* 97, 94–100.
- Rao, R., More, K., Taler, J., Ochoń, P., 2016. Dimensional optimization of a micro-channel heat sink using Jaya algorithm. *Appl. Therm. Eng.* 103, 572–582.
- Rao, Z., Wang, S., Wu, M., Lin, Z., Li, F., 2013. Experimental investigation on thermal management of electric vehicle battery with heat pipe. *Energy Convers. Manage.* 65, 92–97.
- Sahu, R., Sett, S., Yarin, A.L., Pourdeyhimi, B., 2015a. Impact of aqueous suspension drops onto non-wettable porous membranes: hydrodynamic focusing and penetration of nanoparticles. *Colloids Surf. A* 467, 31–45.
- Sahu, R.P., Sinha-Ray, S., Sinha-Ray, S., Yarin, A.L., 2015b. Pool boiling on nano-textured surfaces comprised of electrically-assisted supersonically solution-blown, copper-plated nanofibers: experiments and theory. *Int. J. Heat Mass Transfer* 87, 521–535.
- Sahu, R.P., Sinha-Ray, S., Sinha-Ray, S., Yarin, A.L., 2016. Pool boiling of Novec 7300 and self-rewetting fluids on electrically-assisted supersonically solution-blown, copper-plated nanofibers. *Int. J. Heat Mass Transfer* 95, 83–93.
- Samie, F., Bauer, L., Henkel, J., 2016. IoT technologies for embedded computing: A survey, Proceedings of the Eleventh IEEE/ACM/IFIP International Conference on Hardware/Software Codesign and System Synthesis. *ACM*, p. 8.
- Sankaran, A., Yarin, A.L., 2018. Evaporation-driven thermocapillary Marangoni convection in liquid layers of different depths. *Int. J. Heat Mass Transfer* 122, 504–514.
- Sankaran, A., Zhang, W., Yarin, A.L., 2018. Pool boiling in deep and shallow vessels and the effect of surface nano-texture and self-rewetting. *Int. J. Heat Mass Transfer* 127, 857–866.
- Sevinchan, E., Dincer, I., Lang, H., 2018. A review on thermal management methods for robots. *Appl. Therm. Eng.* 140, 799–813.
- Shahil, K.M., Balandin, A.A., 2012. Thermal properties of graphene and multilayer graphene: Applications in thermal interface materials. *Solid State Commun.* 152, 1331–1340.
- Shtein, M., Nativ, R., Buzaglo, M., Regev, O., 2015. Graphene-based hybrid composites for efficient thermal management of electronic devices. *ACS Appl. Mater. Interfaces* 7, 23725–23730.
- Sinha-Ray, S., Sinha-Ray, S., Yarin, A.L., Weickgenannt, C.M., Emmert, J., Tropea, C., 2014. Drop impact cooling enhancement on nano-textured surfaces. Part II: Results of the parabolic flight experiments [zero gravity (0g) and supergravity (1.8 g)]. *Int. J. Heat Mass Transfer* 70, 1107–1114.
- Sinha-Ray, S., Yarin, A.L., 2014. Drop impact cooling enhancement on nano-textured surfaces. Part I: Theory and results of the ground (1 g) experiments. *Int. J. Heat Mass Transfer* 70, 1095–1106.
- Sinha-Ray, S., Zhang, W., Sahu, R.P., Sinha-Ray, S., Yarin, A.L., 2017a. Pool boiling of Novec 7300 and DI water on nano-textured heater covered with supersonically-blown or electrospun polymer nanofibers. *Int. J. Heat Mass Transfer* 106, 482–490.
- Sinha-Ray, S., Zhang, W., Stoltz, B., Sahu, R.P., Sinha-Ray, S., Yarin, A.L., 2017b. Swing-like pool boiling on nano-textured surfaces for microgravity applications related to cooling of high-power microelectronics. *npj. Microgravity* 3, 1–9.
- Sinha-Ray, S., Zhang, Y., Yarin, A.L., 2010. Thorny devil nanotextured fibers: the way to cooling rates on the order of 1 kW/cm². *Langmuir* 27, 215–226.
- Song, N.-J., Chen, C.-M., Lu, C., Liu, Z., Kong, Q.-Q., Cai, R., 2014. Thermally reduced graphene oxide films as flexible lateral heat spreaders. *J. Mater. Chem. A* 2, 16563–16568.
- Staszal, C., Sinha-Ray, S., Yarin, A.L., 2019. Forced vibration of a heated wire subjected to nucleate boiling. *Int. J. Heat Mass Transfer* 135, 44–51.
- Staszal, C., Yarin, A.L., 2018. Exponential vaporization fronts and critical heat flux in pool boiling. *Int. Commun. Heat Mass Transfer* 98, 171–176.
- Wang, H., Liserre, M., Blaabjerg, F., 2013. Toward reliable power electronics: Challenges design tools and opportunities. *IEEE Ind. Electr. Magazine* 7, 17–26.
- Wang, P., Bar-Cohen, A., 2007. On-chip hot spot cooling using silicon thermoelectric microcoolers. *J. Appl. Phys.* 102, 034503.
- Weickgenannt, C.M., Zhang, Y., Lembach, A.N., Roisman, I.V., Gambaryan-Roisman, T., Yarin, A.L., Tropea, C., 2011. Nonisothermal drop impact and evaporation on polymer nanofiber mats. *Phys. Rev. E* 83, 036305.
- Xu, J., Munari, A., Dalton, E., Mathewson, A., Razeeb, K.M., 2009. Silver nanowire array-polymer composite as thermal interface material. *J. Appl. Phys.* 106, 124310.
- Yarin, A.L., Roisman, I.V., Tropea, C., 2017. *Collision Phenomena in Liquids and Solids*. Cambridge University Press.
- Yu, A., Ramesh, P., Itkis, M.E., Bekyarova, E., Haddon, R.C., 2007. Graphite nanoplatelet– epoxy composite thermal interface materials. *J. Phys. Chem. C* 111, 7565–7569.
- Zhang, H., Shao, S., Xu, H., Zou, H., Tian, C., 2014. Free cooling of data centers: A review. *Renew. Sustain. Energy Rev.* 35, 171–182.
- Zhang, Y.-F., Ren, Y.-J., Bai, S.-L., 2018. Vertically aligned graphene film/epoxy composites as heat dissipating materials. *Int. J. Heat Mass Transfer* 118, 510–517.
- Zhang, Y., Han, H., Wang, N., Zhang, P., Fu, Y., Murugesan, M., Edwards, M., Jeppson, K., Volz, S., Liu, J., 2015. Improved heat spreading performance of functionalized graphene in microelectronic device application. *Adv. Func. Mater.* 25, 4430–4435.
- Zuo, Z.J., North, M.T., Wert, K.L., 2001. High heat flux heat pipe mechanism for cooling of electronics. *IEEE Trans. Compon. Packag. Technol.* 24, 220–225.